Vapor-Liquid-Solid (VLS) Mechanism

Wagner & Ellis, APL '64

950°C, $SiCl_4 + H_2$

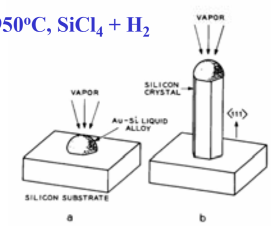

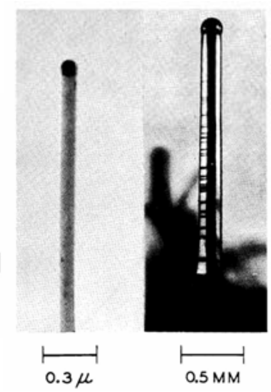

microscopic whiskers and needles

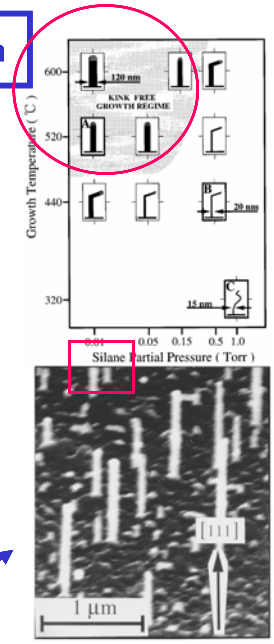

Westwater et al, JVST '97

Laser Ablation VLS

Morales et al, Science 1998

Binary Phase Diagram

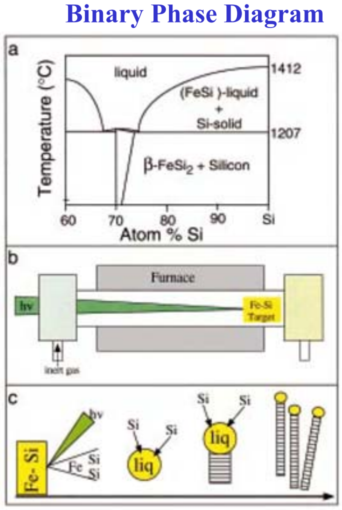

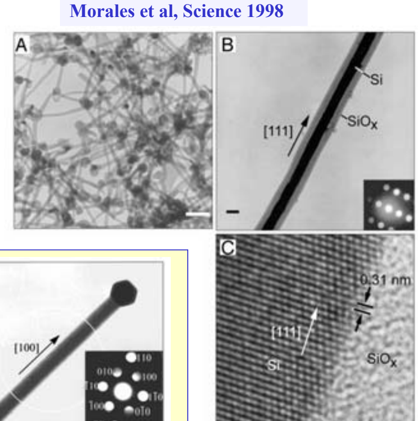

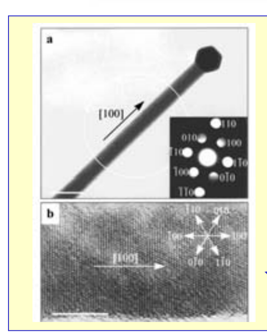

GaN

Oven Growth of GaN

ElAhl et al, JAP 2003

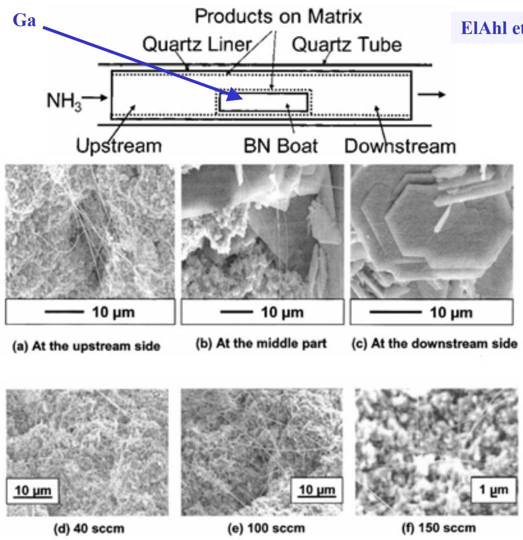

VPE Growth of InAs Nanowires/rods

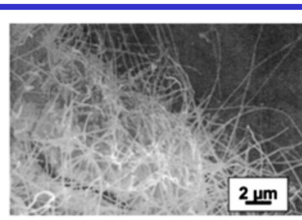

FIG. 2. SEM image of InAs nanowires grown at a N_2 flow rate of 50 sccm, a pressure of 200 Torr, and a temperature of 570 °C for 6 h, and then 500 °C for 30 h.

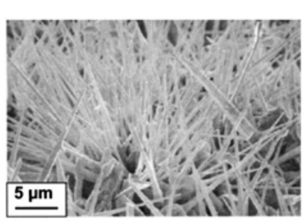

FIG. 3. SEM image of InAs whiskers grown at a temperature of 570 °C, a N_2 flow rate of 50 sccm, and a pressure of 200 Torr for 36 h.

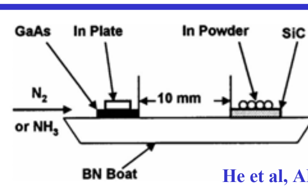

He et al, APL 2003

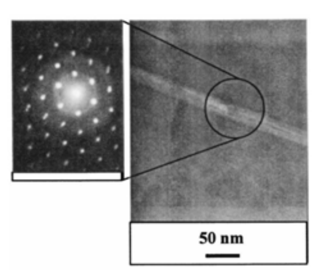

FIG. 5. TEM image of an InAs nanowire grown under the same conditions as those in Fig. 2. The image on the left-hand side shows the selected-area electron diffraction pattern (111) of the nanowire produced in the growth direction [110]. Diffused rings are from the surrounding carbon coating of the sample holder.

Seeded Growth

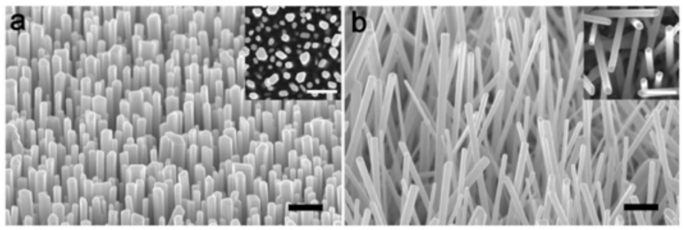

Figure 4. Gas-phase growth of oriented ZnO nanowires on nonepitaxial substrates. (a) ZnO nanowires grown on a silicon (100) surface from acetate-derived seeds; image taken at a 45° tilt. Inset is a plan-view image. (b) ZnO nanowires grown on the same surface without seeds (but with gold catalyst), imaged at a 45° tilt. Inset is a plan-view image. All scale bars are one micron.

Greene et al, Nano Lett. 2005

ZnO Nanowires on Al_2O_3

Huang et al, Science 2001

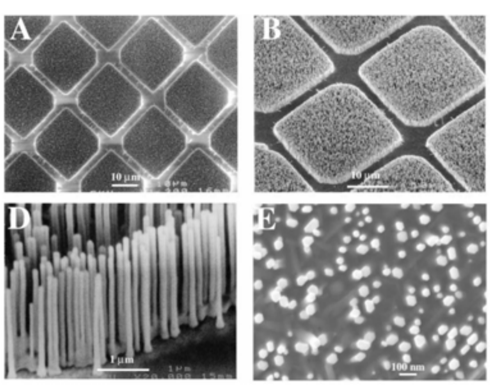

Sapphire, with Au pattern, was placed in close proximity to a boat containing ZnO powder in furnace (Ar).

catalyst-free

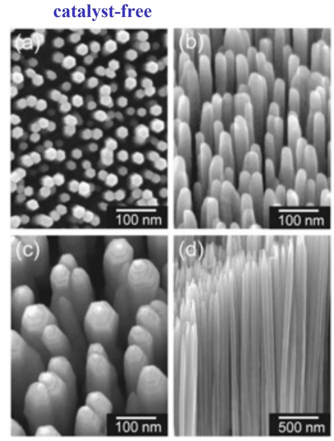

Park et al, APL 02 MOVPE DEZn, O_2, Ar

Initial LT Growth (coarsening) before 400-500^{o}C growth.

VLS Growth With Gold Eutectic

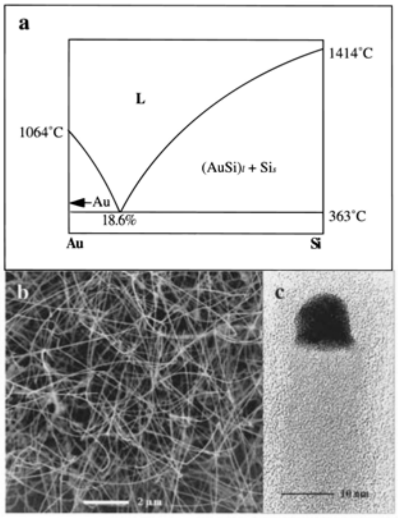

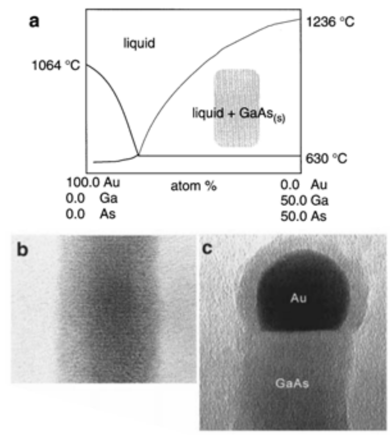

Hu et al, ACR 1999

Ge Nanorods on Si(111)

Au particles

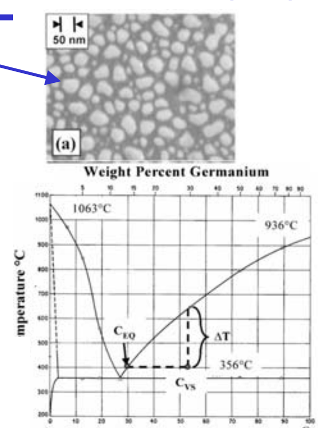

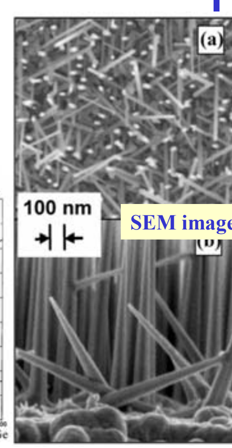

SEM images

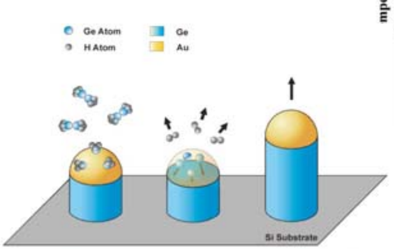

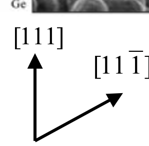

Nanowires On Step Edges

Lin et al, APL 2001

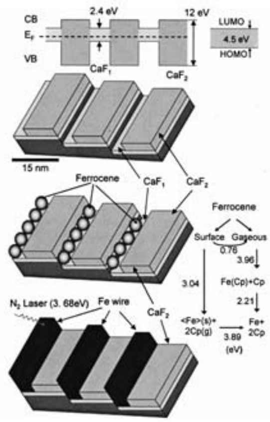

FIG. 1. Schematic of the self-assembly of Fe nanowires on stepped Si with a CaF_2 mask. (Top) Band gap modulation with a periodicity of 15 nm. CaF_1 has states that can interact with the highest occupied and lowest unoccupied orbitals of adsorbed ferrocene (HOMO and LUMO), CaF_2 does not. (Second) CaF_2 stripes on a CaF_1/Si(111) surface obtained at a CaF_2 exposure between 1 and 2 monolayers. The CaF_2 stripes are attached to the upper step edges. (Third) (Left) Selective deposition of ferrocene in the CaF_1 trenches. (Right) Diagrams of energetics of ferrocene on the surface and in the gas phase. (Bottom) Deposition of Fe wires in the CaF_1 trenches after photolysis of adsorbed ferrocene. (Cp=cyclopentadienyl).

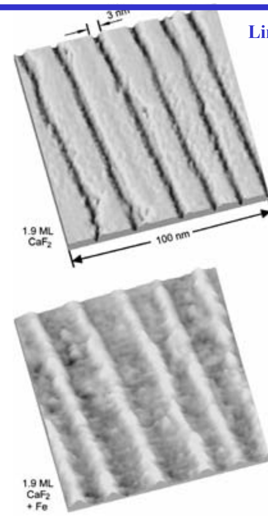

FIG. 2. STM images of the initial and final stages in the self-assembly of Fe nanowires. (Top) Wide CaF_2 stripes separated by narrow CaF_1/Si(111) trenches at a coverage of 1.9 monolayers of CaF_2. (Bottom) Linear array of Fe nanowires 3 nm wide and 0.8 nm thick, selectively deposited in the trenches by photolysis of ferrocene: 100×100 nm^2.

Strain Anisotropy

Chen et al, JAP 2002

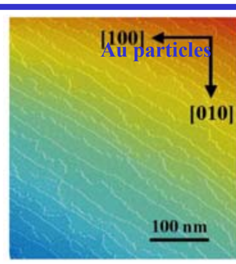

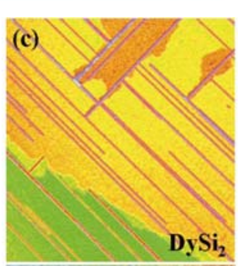

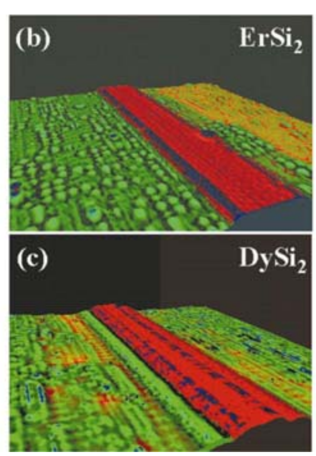

Nanorods, Nanowires

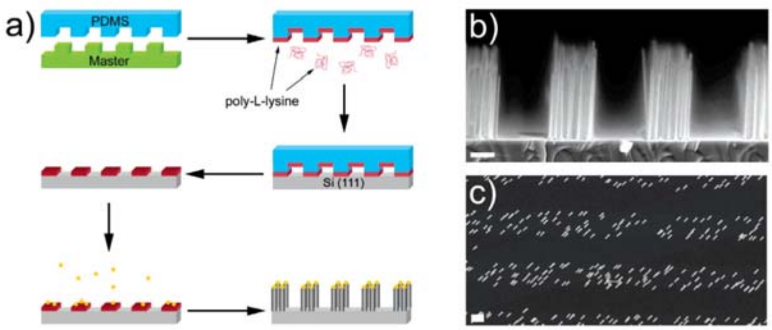

Figure 3. (a) Schematic of PDMS patterning of Au colloids. Briefly, a PDMS stamp is molded to the relief pattern of a photoresist master After curing the polymer, the stamp is removed from the master and "inked" with a solution of poly-L-lysine. The stamp pattern is transferre to the Si (111) substrate, which is then immersed in the Au colloid solution. The colloid-patterned substrate is grown using the conventiona VLS−CVD synthesis, resulting in a corresponding pattern of SiNW arrays. (b) Cross-sectional SEM image of PDMS patterned SiNW growth, and (c) plane-view SEM image of the same. Scale bars are 1 μm.

Hochbaum et al, Nano Lett. 2005

Nanowires

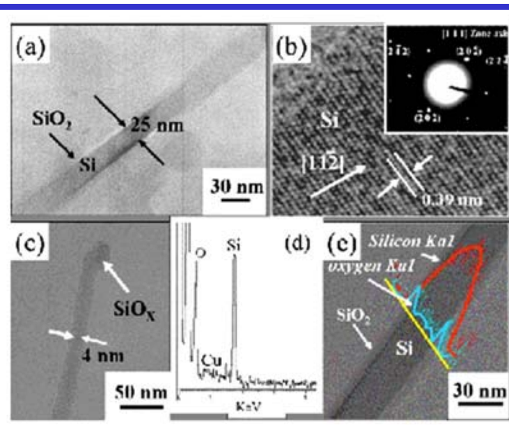

FIG. 2. (a) TEM image of taperlike Si nanowires. (b) High-resolution TEM image of a taperlike SiNW. The growth direction is along [11$\bar{2}$] direction. Inset shows the selective area diffraction pattern with [111] zone axis. (c) TEM image of taperlike SiNWs for the tip area shows that it is free of metal catalyst. (d) The EDS spectrum for the tip region. (e) The EDS line profile of the taperlike SiNW.

Chueh et al, APL 05

Colloids

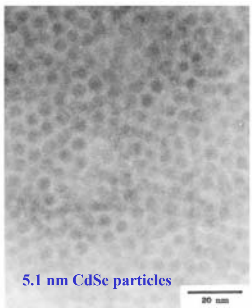

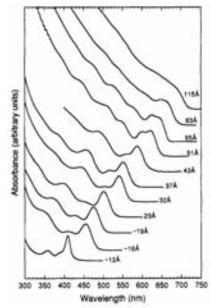

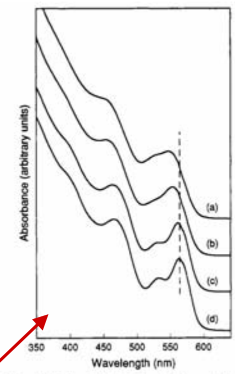

Figure 1. Example of the effect of size-selective precipitation on the absorption spectrum of ~37 Å diameter CdSe nanocrystallites. (a) Room temperature optical absorption spectrum of the nanocrystallites in the growth solution before size-selective precipitation. (b) Spectrum after one size-selective precipitation from the growth solution with methanol. (c) Spectrum after dispersion in 1-butanol and size-selective precipitation with methanol. (d) Spectrum after a final size-selective precipitation from 1-butanol/methanol.

Murray et al, JACS 1993

* To achieve monodispersed CdSe (CdS, CdTe) quantum dots, organometallic reagents are rapidly injected into a hot coordination solvent to induce short burst of nucleation. Subsequent slow growth (Ostwald ripening) leads to dots uniform in size.
* Can monitor the absorption spectrum to adjust the temperature (distribution broadens → lower T). Can extract particles of different sizes after different growth times. Certain "favorite sizes" exist.
* Colloid surfaces are capped for controlled growth and repulsion between particles. Chemicals can be added to increase the solvent polarity which reduces barrier to flocculation, especially for larger particles. Flocculate can be removed and dispersed. Supernatant can again flocculate for finer size selection.

Colloidal Nano-particles

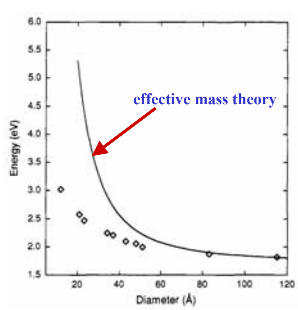

HOMO-LUMO gap

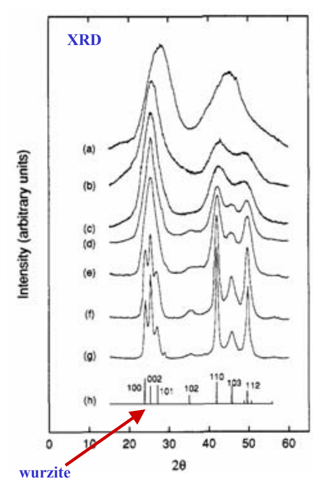

Murray et al, JACS 1993

Plasma Enhanced CVD Quantum Dots

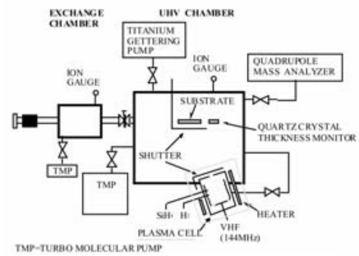

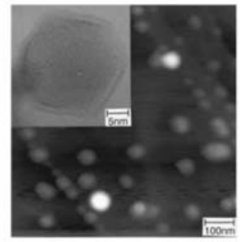

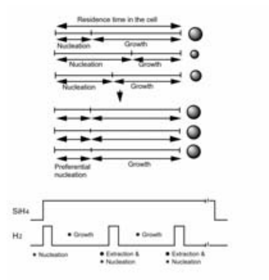

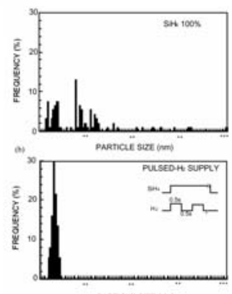

Oda et al, JP 2001

Buckminsterfullerines C_{60}

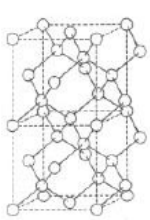

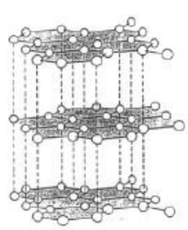

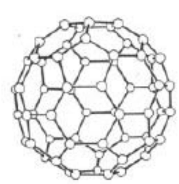

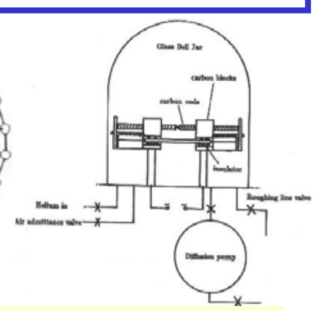

Now form of carbon. C_{60} structure consists of 12 pentagons and 20 hexagons. 120 symmetry operations! Chemically stable.

Easy to fabricate. Use arc machine to produce black soot in inert gas. Use chromatography to separate out C_{60} (with some C_{70} and C_{78}) in solvents.

The discovery of C_{60} in 1985 led to a Nobel prize in chemistry for Curl, Kroto, and Smalley in 1996.

Fullerene Chemistry

fullerene family

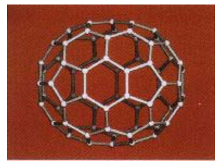

C_{70}

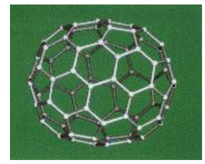

C_{76}

fullerene compounds (>9,000)

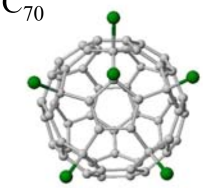

$C_{60}Cl_6$

fullerene solid (f.c.c) &

alkali-doped fullerides

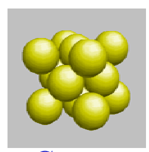

C_{60}

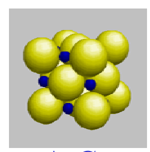

A_1C_{60}

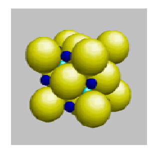

A_3C_{60}

Quick Facts About Carbon Nanotubes (CNT)

1. A new form of carbon, first discovered in 1991. Instantly became a model self-assembled 1D system for "nano-scientists". As of 2005, more than 1300 papers have been published and 120 patents on the fabrication of CNT have been filed.

2. Potential applications in composite polymer materials, high-capacity battery electrode (Li-intercalated), field emitters, nano-electronics, nano-sensors, catalyst for oxygen reduction (fuel cells), hydrogen storage media.

3. Various structures from small as 0.42 nm diameter. Can be metallic or semiconducting, depending on chirality.

4. Good ballistic transport properties, high thermal conductivity and optical polarizability.

5. Main methods of fabrication: laser ablation, arc-discharge, CVD.

What are carbon nanotubes?

carbon nanotube: rolled-up sheet of graphene

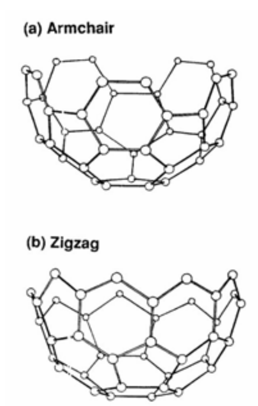

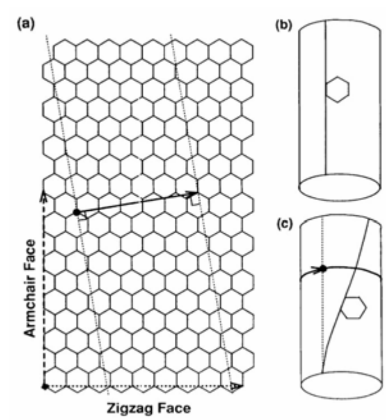

Can be viewed as "elongated fullerenes" e.g. C_{60+10j}, C_{60+18j}, C_{78+4j}, ...

Early Growth of CNT

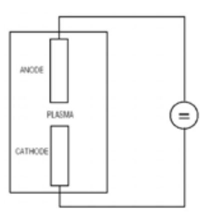

Iijima Nature 1991

ARC DISCHARGE

graphite electrodes (gap ~ a few mm)

dc arc discharge (typically 100A, 30V, a few minutes)

pressure 10-760 Torr Ar, He, etc. (CH_4)

MWNT grown from cathode (soot all over chamber, spider webs, spaghetti, etc.)

SWNT with metal catalysts (powder placed in hole drilled in anode)

flowing Ar

cold collector

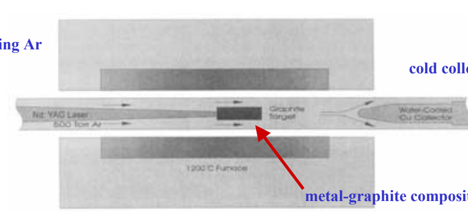

metal-graphite composite

Guo et al, JPC 1995

Laser Ablation

CVD Fabrication of SWNT

bimetallic Mo/Fe nanocluster catalyst

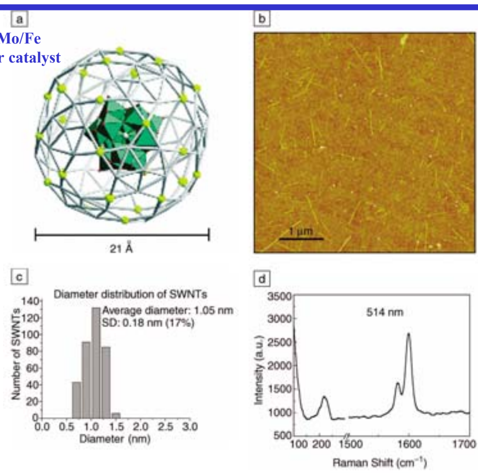

Figure 2. (a) Structure of a metal-containing molecular nanocluster found to be a good catalyst for chemical vapor deposition growth of single-walled carbon nanotubes (SWNTs). The icosahedral capsule comprises 30 Fe atoms (yellow atoms) connected with the 12 (Mo)Mo_5 pentagons, and the reduced Keggin nucleus containing 12 Mo atoms is in the center. (b) Atomic force microscopy (AFM) image of SWNTs grown using the molecular nanocluster as a catalyst. (c) Diameter distribution of SWNTs grown on chemically attached Fe/Mo nanoclusters on silicon dioxide surfaces. (d) Raman spectrum of SWNTs thus grown, showing a size range in good agreement with AFM measurements.

- methane CVD
- HiPCO
- CO CVD
- alcohol CVD

Liu et al, MRSB 2004

Catalyst-Aided SWNT Growth: Tip Growth

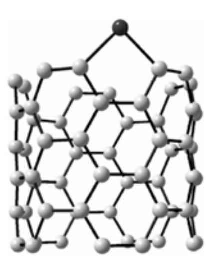

SWT growth involves at least one open end. Metal atoms (Ni) inhibits the formation of pentagons which initiate the closure of the open ends of CNT. Ni-C bond strength is strong to be comparable to carbon bonds in nanotube (also so that it doesn't desorb easily), yet still mobile to anneal defects before they are incorporated in the growing structure.

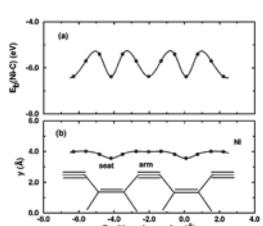

Binding energy and equilibrium height of Ni to the edge of an armchair CNT.

Lee, et al, PRL 97

SWNT Growth: Base Growth (Root Growth)

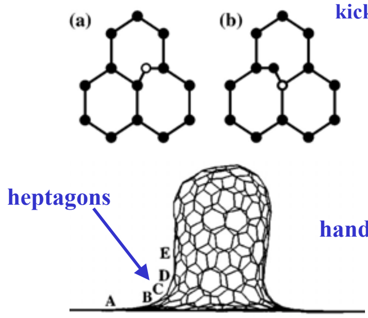

Handle site	Energy
A	0.0
B	−0.1
C	−0.5
D	−0.2
E	0.05

Maiti, et al, PRB 97

kick-out mechanism

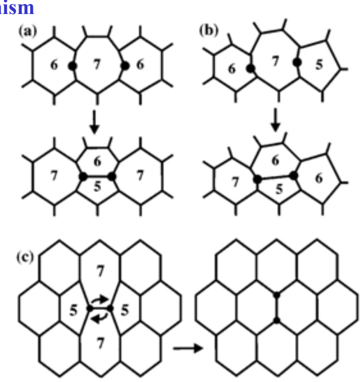

Carbon atoms dissolve in metal particles then precipitate out.

Capped Ends of Nanotubes

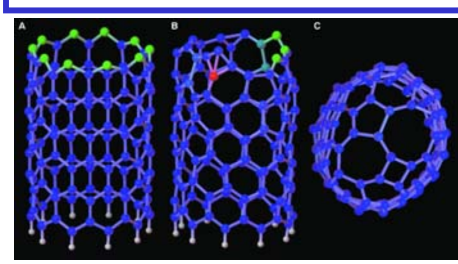

pentagons and heptagons

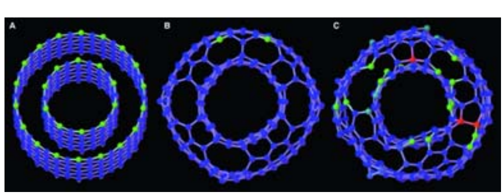

Lip-lip interaction stabilizes the open-ended growth. Bridging bonds continuously break and re-form to facilitate the rapid absorption of carbon atoms.

Chirality Of CNT

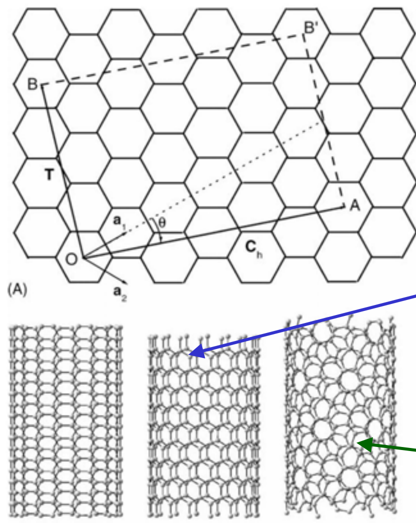

graphene

$d_{C\text{-}C}$ = 0.142 nm

$C_h = na_1 + ma_2$ (chirality vec.)

radius = $C_h/2\pi$

zig-zag

(n, 0)

θ = 0º

armchair

(n, n)

θ = 30º

chiral (no mirror symm.)

(n, m)

Electronic Structure of CNTs

bonds and bands of various forms of carbon:

Four valence electrons per atom.

Common bonding configuration sp_3 and sp_2.

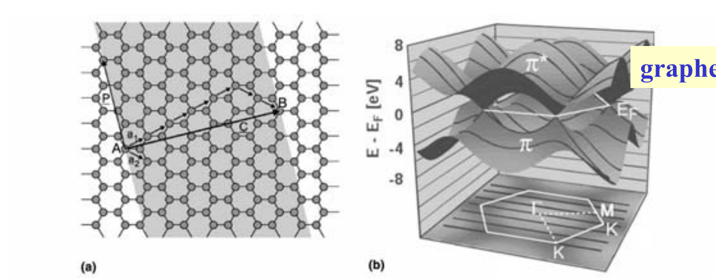

graphene sheet

Avouris, CP 2002

Fig. 1. (a) Schematic illustration of the generation of a nanotube by folding of a section of a graphene sheet. The folding and the resulting nanotube can be characterized by a chirality vector $\underline{C} = n\underline{a}_1 + m\underline{a}_2 \equiv (n, m)$, where $\underline{a}_1$ and $\underline{a}_2$ are the unit vectors of the hexagonal lattice. When point B is brought over point A a tube with a circumference C is generated. In the example shown $\underline{C} = 5\underline{a}_1 + 2\underline{a}_2$, and the tube is labeled as (5, 2). (b) Top: Band-structure of the 2D graphene sheet (in gray). The valence and conduction bands meet at six points (K-points) lying at the Fermi energy. Bottom: The first Brillouin zone of graphene. The black lines represent the states of a (3, 3) nanotube. They are cuts of the graphene structure that are selected by imposing the condition that the perpendicular wavevector $\underline{k}_C$ satisfies the condition: $\underline{k}_C \cdot \underline{C} = 2\pi j$, where j is an integer. If the states pass through a K-point (as in this case) the tube is a metal, while if they do not, the tube is a semiconductor.

Chirality and "Band Gap" of CNT

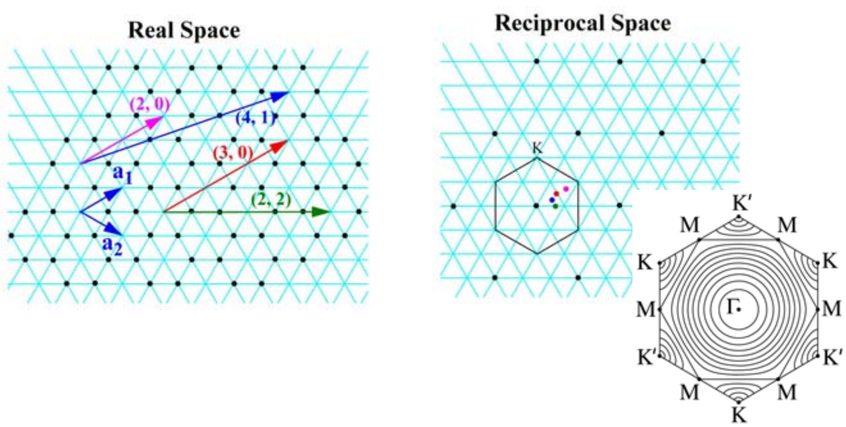

(n, m) CNT is metallic when n-m = 3j, where j is integer
(n, m) CNT is semiconducting when n-m = 3j + 1, or 3j + 2

SWCNT Band Structure

Let $a_1 = a(1,0)$ and $a_2 = a(1/2, -\sqrt{3}/2)$. The chirality vector for a (3n, 0) CNT is at (3na, 0). The reciprocal vector is at (2π/a)(1/3n, 0). Since K-point and K'-point, where the π and π* band touch, are at positions 2π(1/3a, $\pm\sqrt{3}$/3a) and (4π/3a, 0) in the reciprocal lattice, CNT with (3n, 0) chirality vector obviously cuts through K(K')-point. Also, (n, n) chirality vector cuts through the K(K') point. Let's calculate for CNTs with chirality vector (3+n, n), which has a length of $a\sqrt{(3+n+n/2)^2+3n^2/4}$ and is at an angle of $\tan^{-1}\left(-\frac{n\sqrt{3}/2}{3+1.5n}\right)$. The length of the reciprocal space vector is 2π/($a\sqrt{(3+1.5n)^2+3n^2/4}$). The coordinates in reciprocal space is (2π/a) $\left[(3+1.5n)^2+3n^2/4\right]^{-1}\left(3+1.5n, -n\sqrt{3}/2\right)$. The distance between K-point and Γ-point is 4π/(3a). Use the Pythagorean theorem to verify that the angle between the line containing K(K')-point and the chiral reciprocal vector and the line containing reciprocal chiral vector and the origin is indeed a right angle. We have, neglecting a factor of 2π/a,

$$\left(\frac{1}{3}-\frac{3+1.5n}{9+3n^2+9n}\right)^2+\left(\frac{\sqrt{3}}{3}+\frac{n\sqrt{3}/2}{9+3n^2+9n}\right)^2+\frac{1}{9+3n^2+9n}=\frac{4}{9}.$$

Indeed, this angle is a right angle because 4/9 is the square of 2/3. Using similar method, it can be shown that folding with chirality vector (2+n, n) or (1+n, n) fails to include K and K' points on the 1D band diagram.

Electronic Structure & Optical Properties

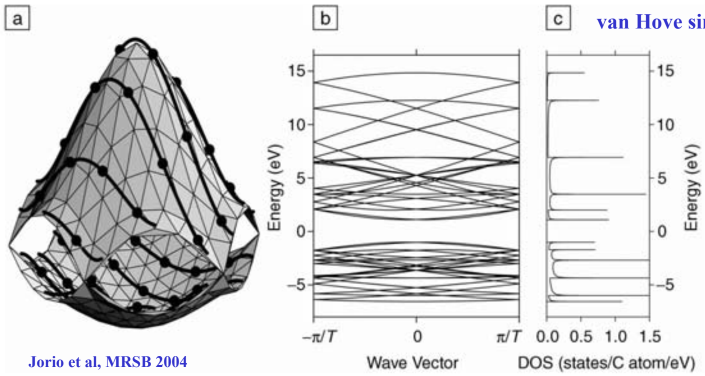

Figure 1. (a) The calculated constant-energy contours for the conduction and valence bands of a graphene layer in the first Brillouin zone using the π-band nearest-neighbor tight-binding model.[3] Solid curves with dots show the cutting lines for the (4,2) nanotube.[6] (b) Electronic energy band diagram for the (4,2) nanotube obtained by zone-folding from (a). T gives the length of the nanotube unit cell along the tube axis. (c) Density of electronic states for the band diagram shown in (b).

van Hove singularities

$$dN = \left(\frac{L}{\pi}\right) dk$$

free electrons

$$k = \frac{\sqrt{2m(E - E_0)}}{\hbar}$$

$$dk = \frac{dE}{\hbar}\sqrt{\frac{m}{2(E - E_0)}}$$

Optical Determination of CNT Chirality

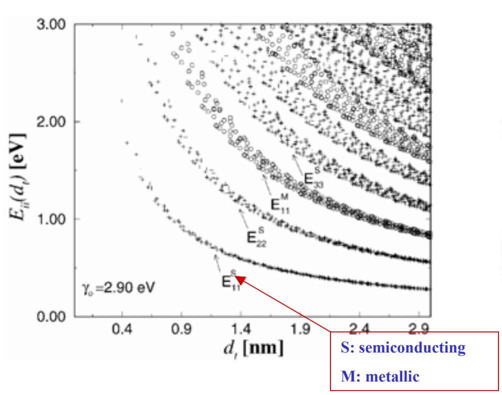

selection rules

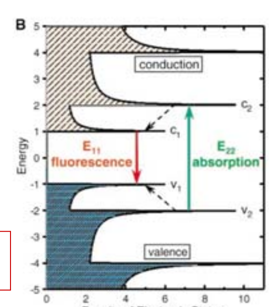

"Kataura" plot

Filho et al, NT 2003

Fluorescence Spectroscopy

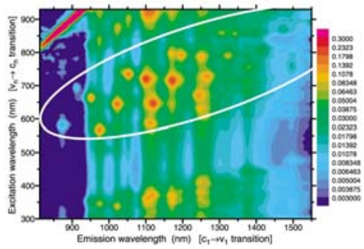

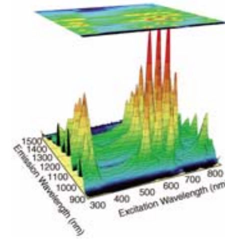

band gap ~ 0.9 eV/d (dia. in nm)

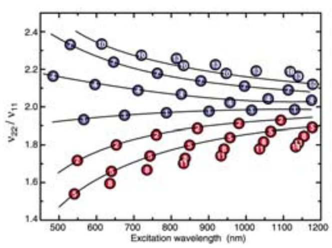

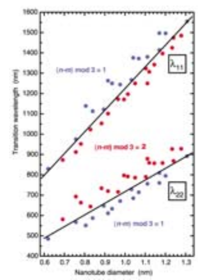

Bachilo, Science 2002

Measuring Diameter of SWNT

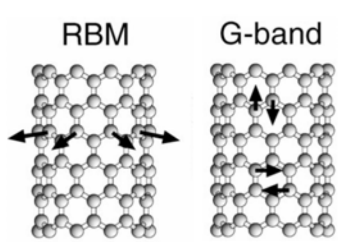

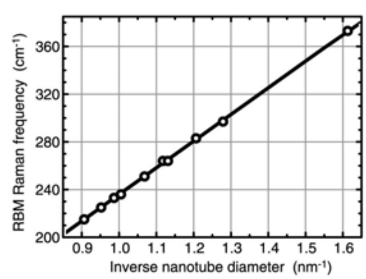

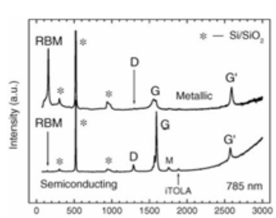

Isolation of Individual SWNT

Aggregates and bundles conceal the property of individual SWNTs.

Need to separate out individual tubes and prevent them from reattaching.

Vigorous sonication in aqueous solution with surfactant, followed by centrifuging, leading to micelle-suspended nanotubes. (SDS = sodium dodecyl sulfate)

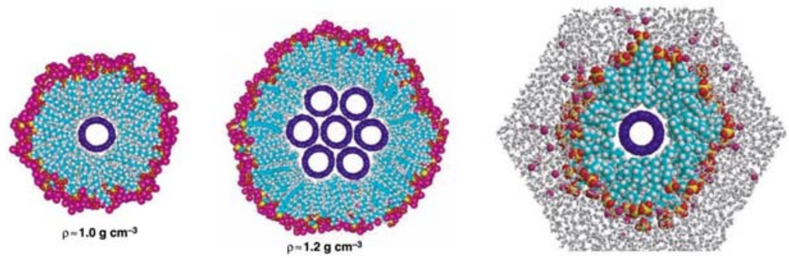

O'Connell et al, Science 2002

Preferential Deposition of Metallic SWNTs

Rayleigh scattered light from the dielectrophoretically deposited SWNTs and the electrodes, recorded with an incident-light dark-field microscope. The scattered light from the aligned SWNTs appears green to the eye (A) and is polarized perpendicular to the electrodes (B).

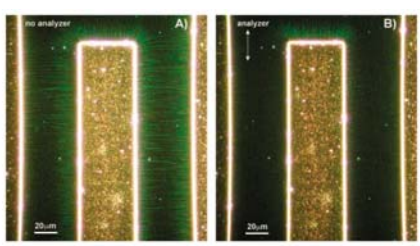

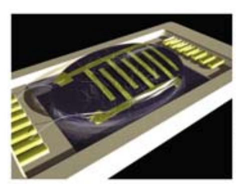

Fig. 1. Illustration of the experimental setup, showing microelectrodes wired to a chip carrier. The metallic nanotubes (black) are deposited from a drop of nanotube suspension onto the electrodes by ac dielectrophoresis, leaving the semiconducting tubes (white) in suspension. Gold electrodes are 30 nm thick and 50 μm wide, with a 50-μm pitch on a p-type silicon substrate with 600 nm of thermally oxidized SiO_2. A thin Ti adhesion layer was used.

AC Electrophoresis.
Krupke, et al Science 2003

Raman spectra of SWNTs deposited via ac dielectrophoresis compared to a reference sample deposited on Si without the application of an electric field. RBMs associated with metallic (blue) and semiconducting (red) SWNTs.

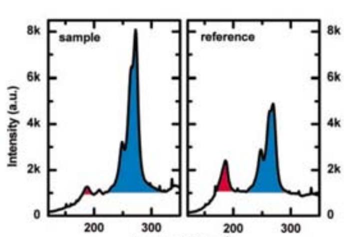

electrophoresis: the movement of suspended particles through a fluid or gel under the action of an electromotive force applied to electrodes in contact with the suspension

Selecting Semiconducting CNTs

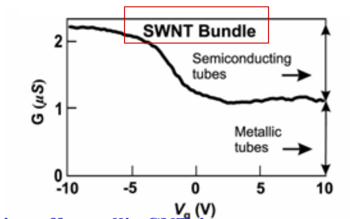

AFM after before

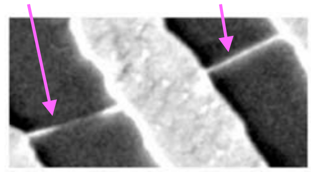

burning off metallic CNTs!

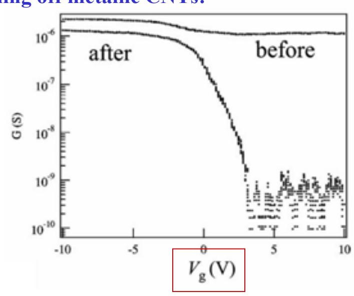

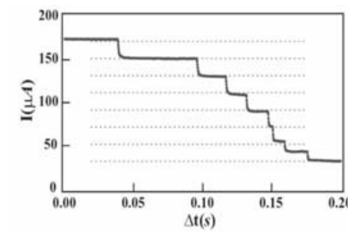

Fig. 5. Time-dependence of the current flowing through a multi-walled nanotube during current-induced breakdown.

Avouris, CP 2002

Gas Storage & Peapods

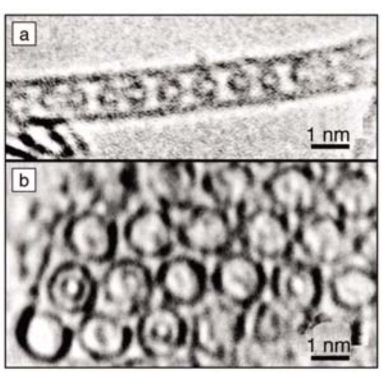

AG: as grown (closed ends)
HT: heat treated (open ends)

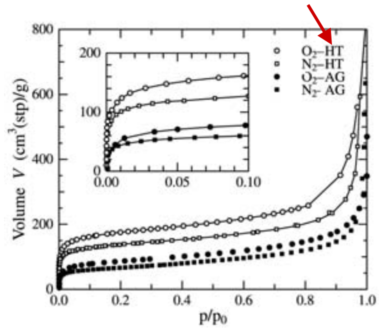

Sloan, et al, MRS Bull. 2004

Fujiwara et al, CPL2001

CNT FETs

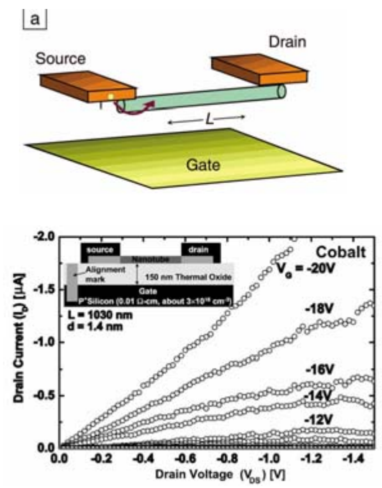

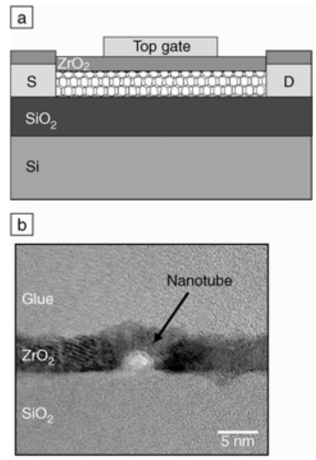

Doping of SWCNT

doping of semiconducting SWNT

K, O_2,

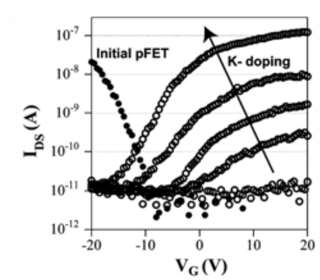

Fig. 13. Changing output characteristics of an initially p-type carbon nanotube field-effect transistor exposed to increasing amounts of potassium.

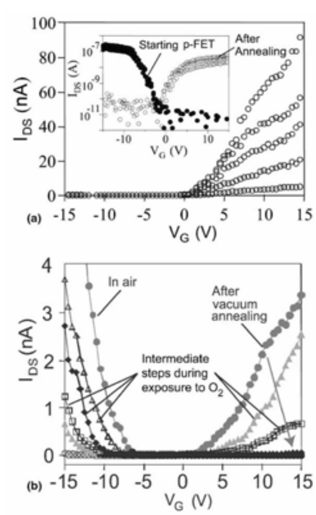

SWNT p-n Junction

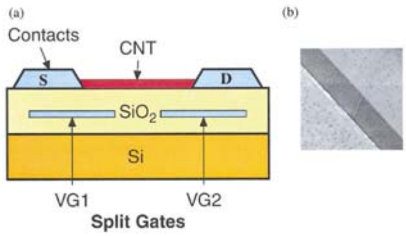

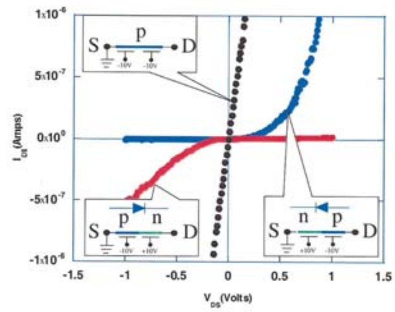

Lee et al, APL2004

Transport Properties of SWNT

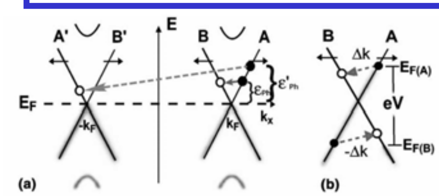

applied bias

$$E_{ph} = \hbar c_{ph} k_{ph}$$

10^4 m/s

For metallic SWNT, the graphene K and K' belong to the 1D Brillouin zone. There are two modes with linear dispersion (zero mass) crossing the Fermi energy at k_F and $-k_F$. One mode involves electrons moving to the right and the other electrons moving to the left.

There is nearly ballistic transport in metallic SWNT because of very limited phase space for scattering event. Optical phonons are inaccessible at RT. Intraband (A -> A') acoustic phonon scattering is also unimportant. Only interband (A -> B) transitions are allowed, however, there are strict selection rules on the type of phonons. There is however, electron-electron scattering.

Avouris, Chem. Phys. 2002

Transport Properties of SWNT

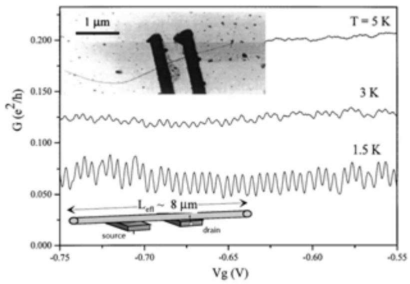

metallic

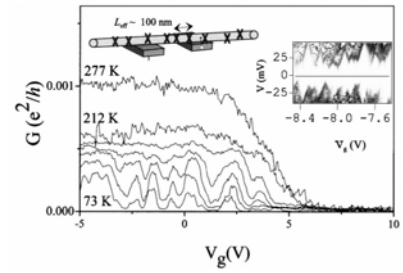

semiconducting

McEuen, et al, PRL 99

Coulomb Blockade

$$E_c = \frac{Q^2}{2C_\Sigma}$$

example: metal sphere

$$C = 4\pi\varepsilon_0 R \qquad E = \frac{1}{4\pi\varepsilon_0}\frac{Q^2}{2R}$$

When objects get smaller, the charging energy can exceed thermal energy. If electrons are to tunnel onto the island, the capacitor must be charged. Therefore a threshold bias voltage is needed for electron transport. Below this voltage, electron transport is suppressed, as shown in figure, and no current is observed. Only if a larger voltage is applied can electrons tunnel onto the island and further to the other reservoir.

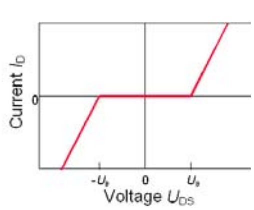

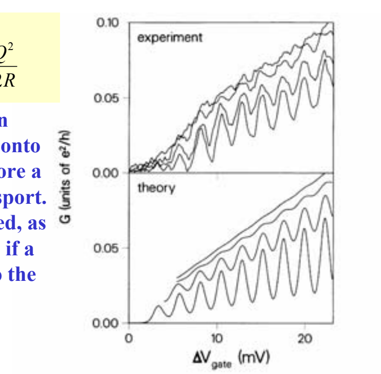

FIG. 4. Top panel: two-terminal conductance vs gate voltage of channel $U3$ for $T = 3.2$, 2.5, 1.6, and 1 K, from top to bottom. Bottom panel: conductance calculated from Eq. (9) for $e^2/C = 0.6$ meV, $\Delta E = 0.1$ meV, $\alpha = 0.265$, $\hbar\Gamma_p^{l,r} = 0.027pE_p$, and twofold degeneracy.

GaAs 2DEG

Staring et al, PRB 1992

Coulomb Blockade

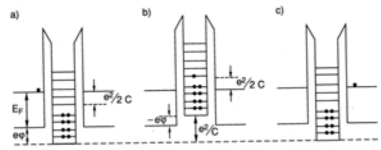

FIG. 3 Single-electron tunneling through a quantum dot, under the conditions of Eq. (2.6), for the case that the charging energy is comparable to the level spacing. An infinitesimally small voltage difference is assumed between the left and right reservoirs.

$$E_N^* \equiv E_N + (N - \tfrac{1}{2})\frac{e^2}{C} = E_F + e\phi_{ext} \qquad (2.6)$$

van Houten, NATO 1992

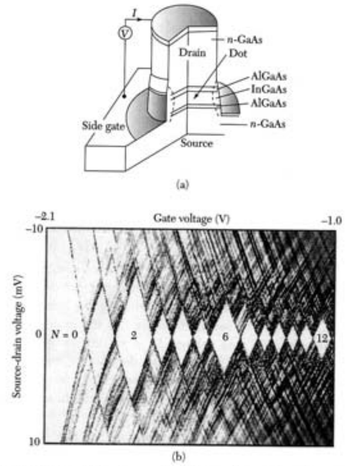

Figure 23 (a) Schematic of a 2D circular quantum dot formed in a GaAs/AlGaAs heterostructure. (b) The differential conductance dI/dV as a function of both gate voltage and source drain bias, plotted as a gray scale. The white diamond regions correspond to different charge states of the dot. A larger charging energy is observed for $N = 2$ and 6 electrons on the dot, corresponding to filled electronic shells. The additional lines on the diagram correspond to excited energy levels of the dot. (Courtesy of L. Kouwenhoven.)

1D Conductance

Ballistic Transport
Conductance Quantization

$$\mu_1 - \mu_2 = eV \qquad v_{\rightarrow} = \frac{1}{\hbar}\frac{dE}{dk}$$

$$I = \int_{\mu_1}^{\mu_2} dE \left(\frac{dn_{\rightarrow}}{dE}\right) e\, v_{\rightarrow}$$

$$\frac{dn_{\rightarrow}}{dE} = \frac{dn_{\rightarrow}}{dk}\frac{dk}{dE} = \sum_{occup.band} \frac{1}{\pi}\frac{dk}{dE}$$

occupied bands

$$I = \int_{\mu_1}^{\mu_2} dE\, \frac{eN}{\pi\hbar} = N\frac{2e^2}{h}V$$

$h/2e^2 = 12.9\ k\Omega$

Landauer formula

$$G = \frac{2e^2}{h}\Im$$

transmission coeff.

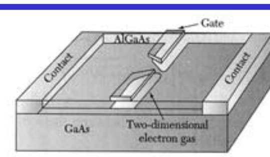

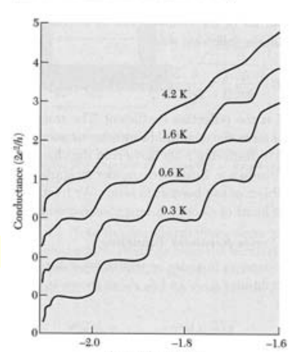

Non-carbon Nanotubes

BN nanotubes

hexagonal BN wide gap
semiconductor (Eg ~ 5.8 eV)

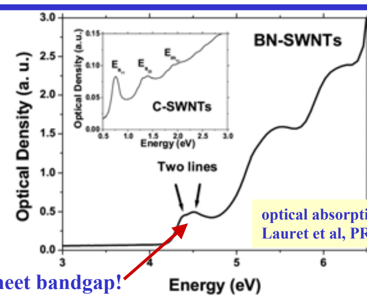

optical absorption
Lauret et al, PRL 2005

below sheet bandgap!

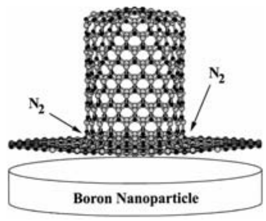

Lee et al, PRB 2001

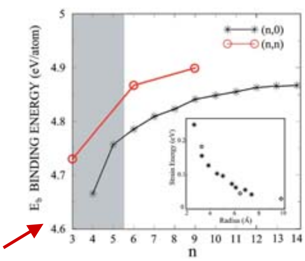

SiNT Durgun et al, PRB 2005

Zeolites

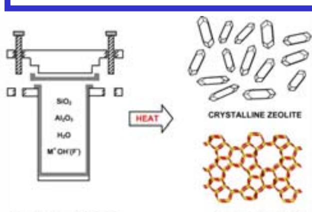

hydrothermal process

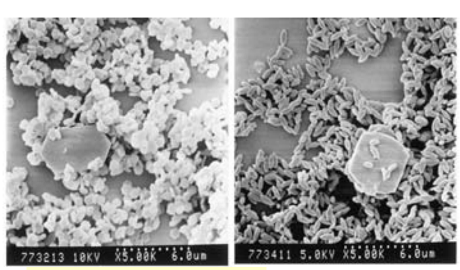

Cundy, Cox, MMM 2005

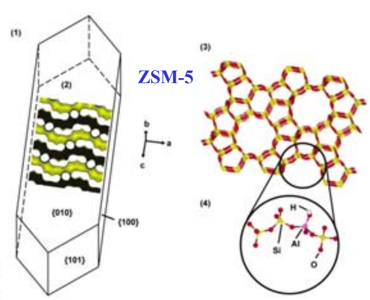

ZSM-5

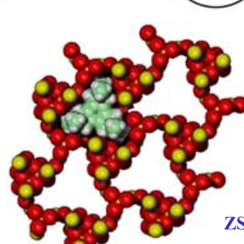

ZSM-18

template molecule

Micro Self-Assembly

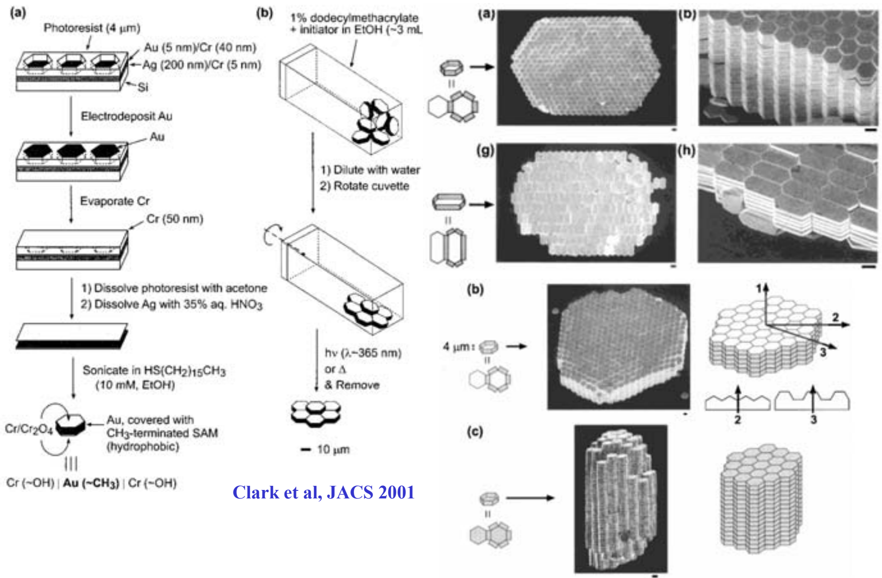

Clark et al, JACS 2001

Evaporation Induced Self Assembly (EISA)

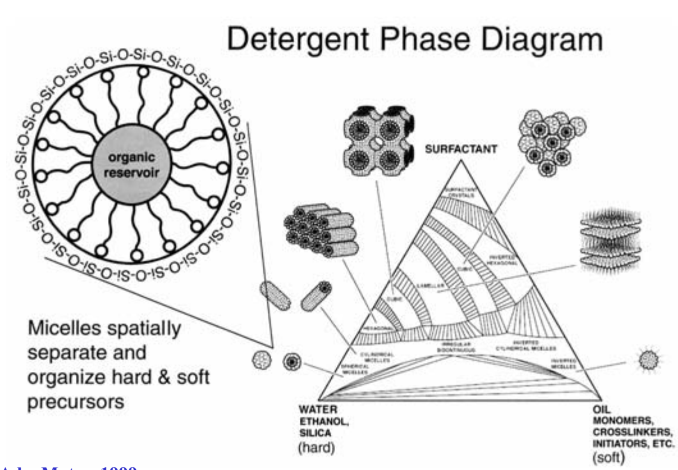

Brinker et al, Adv. Mater. 1999

Self-Assembly of Mesophases

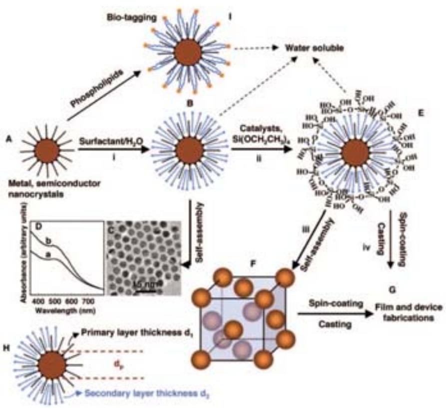

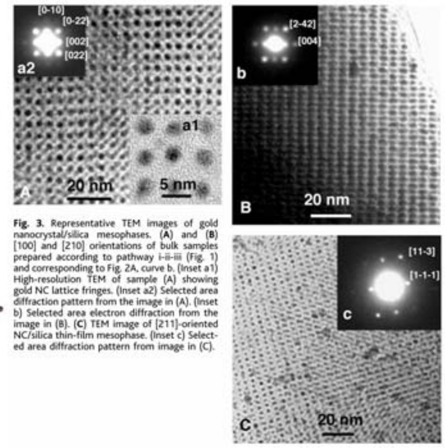

Fig. 3. Representative TEM images of gold nanocrystal/silica mesophases. (A) and (B) [100] and [210] orientations of bulk samples prepared according to pathway i-iii-iiii (Fig. 1) and corresponding to Fig. 2A, curve b. (Inset a1) High-resolution TEM of sample (A) showing gold NC lattice fringes. (Inset a2) Selected area diffraction pattern from the image in (A). (Inset b) Selected area electron diffraction from the image in (B). (C) TEM image of [211]-oriented NC/silica thin-film mesophase. (Inset c) Selected area diffraction pattern from image in (C).

Fan et al, Science 2004

Dip Coating

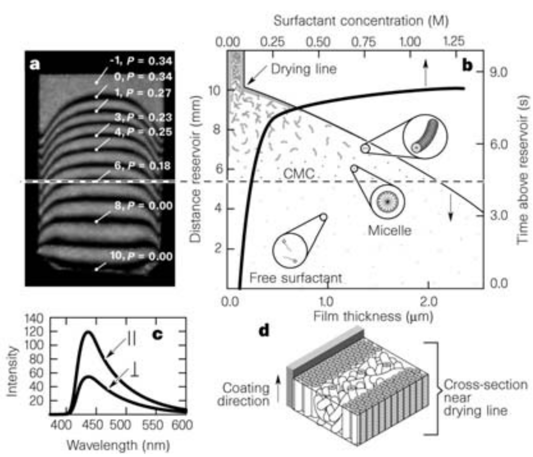

sol-gel dip coating

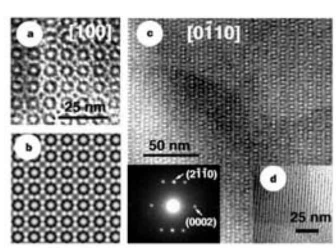

Lu et al, Nature 1997

Aerosol Processing

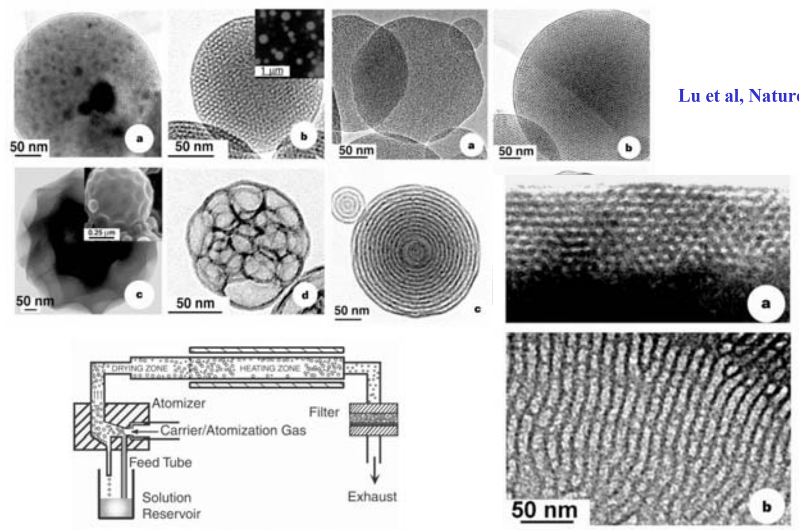

Lu et al, Nature 1999

Modification of Mesophase

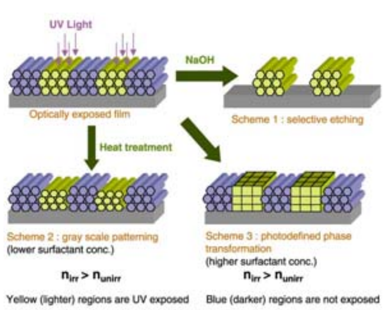

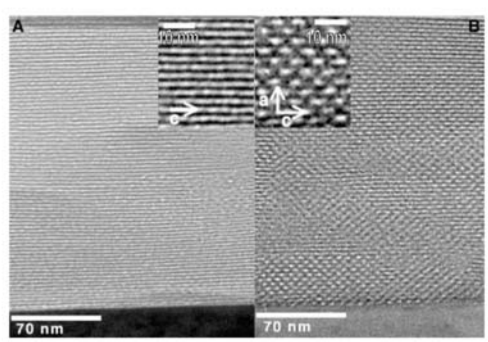

unirradiated irradiated

Doshi et al, Science 2000

Photo-responsive Membrane

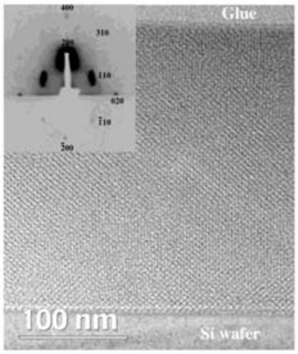

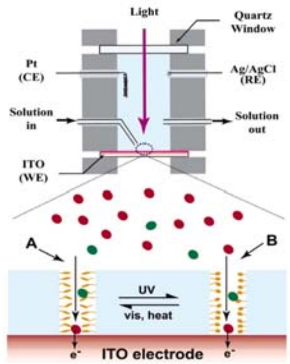

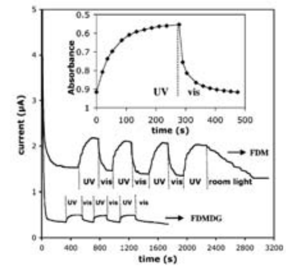

Figure 4. $I-t$ behavior of a photoresponsive nanocomposite film under alternate exposure to UV (360 nm) and visible light (435 nm). (Last cycle uses room light, 400−700 nm.) Inset is the absorbance at 356 nm ($\pi-\pi^*$ transition of the trans isomer) of the same film immersed in the buffer solution containing 1 mM FDM. The time scale of the UV/vis data corresponds to that of the first cycle in the $I-t$ response curve using FDM as the molecular probe.

azobenzene (trans ⇔ cis)

TEOS/TSUA bcc mesostructure

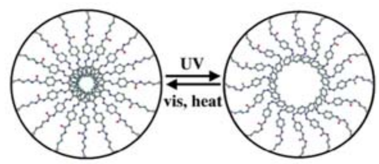

Liu et al, NL 2005